


**Topological classification of nodal-line semimetals in square-net materials**Inho Lee <sup>1</sup>, S. I. Hyun,<sup>1</sup> and J. H. Shim<sup>1,2,\*</sup><sup>1</sup>*Department of Chemistry, Pohang University of Science and Technology, Pohang 37673, Korea*<sup>2</sup>*Department of Physics, Pohang University of Science and Technology, Pohang 37673, Korea*

(Received 25 March 2020; revised 12 January 2021; accepted 9 March 2021; published 6 April 2021)

Fermi surface topology and Berry phase of square-net-layered materials with  $P4/nmm$  space group were classified based on the first-principles analysis of Berry phases in each materials. The variation of electron-hole ( $e-h$ ) asymmetry, driven by the third-nearest-neighbor hoppings of pnictogen  $p_{x,y}$  orbitals in square-net, is essential to yield various topological Fermi surfaces. The change of chemical potential too yields various topological Fermi surfaces. By determining  $e-h$  asymmetry and chemical potential of the reported square-net-layered materials, we construct the phase diagram of the Fermi surface topologies. In addition, we adopt interlayer interaction and investigate three-dimensional Fermi surface. We classify the three-dimensional Fermi surface topologies based on the phase diagram, and our classification reproduces the quantum oscillation and spectroscopy results for various square-net compounds.

DOI: [10.1103/PhysRevB.103.165106](https://doi.org/10.1103/PhysRevB.103.165106)**I. INTRODUCTION**

Dirac materials, hosting pseudorelativistic Dirac fermions with conical energy dispersion, have been actively studied because of their outstanding physical properties like extremely large carrier mobilities, anomalous quantum Hall effects, giant magnetoresistance [1–7]. Following the discovery of graphene with honeycomb lattice, various two-dimensional Dirac materials are investigated, such as silicene with buckled honeycomb structure [8], MoS<sub>2</sub> allotrope with square-octagon structure [9], and FeSn with Kagome lattice [10]. Among the Dirac semimetals, the square-net-layered materials have been investigated since the discovery of highly anisotropic Dirac fermion in SrMnBi<sub>2</sub> [11]. By studying the tight-binding (TB) model, symmetry-protected Dirac points in the square-net-layered semimetals with nonsymmorphic space group have been investigated [12].

The square-net materials are classified into two families by the stacking type of cations neighboring the square net (Fig. 1). First, the  $I4/mmm$  family, including SrMnBi<sub>2</sub> and BaMnBi<sub>2</sub>, has coincident stacking order of cation atoms above and below the square-net layer. Angle-resolved photoemission spectroscopy (ARPES) and Shubnikov-de Haas (SdH) oscillations of the  $I4/mmm$  materials presented the strongly anisotropic Dirac fermions, as confirmed by the density functional theory (DFT) and TB analysis [11,13–15].

On the other hand, the  $P4/nmm$  family, including CaMnBi<sub>2</sub> and ZrSiS, has staggered stacking order of cation atoms. Although there have been intensive experimental investigations on those materials recently, the topological properties of  $P4/nmm$  materials are theoretically less understood. The TB studies of  $P4/nmm$  materials predict the nodal-line features unless the charge density wave (CDW) distortion of square-net layer changes the space group to  $Pnma$ . In addition,

topologically nontrivial states in  $P4/nmm$  materials were observed in SdH oscillation, ARPES, and angular magnetoresistance (AMR). In SdH oscillation, Berry phases were observed to be trivial in LaSbTe [16], but nontrivial in other  $P4/nmm$  materials such as CaMnBi<sub>2</sub> [17], YbMnBi<sub>2</sub> [5,18], YbMnSb<sub>2</sub> [19], HfSiS [20], ZrGeSe [21], ZrGeTe [21], ZrSiSe [22], ZrSiTe [22], ZrSnTe [23], and ZrSiS [22,24]. The unusual butterfly-shaped AMRs were observed in ZrSi(S/Se) [25], in contrast to the typical AMR in ZrSiTe [22]. ARPES studies revealed the tunable Dirac and Weyl states in CeSbTe [26,27], the anisotropic Fermi surfaces of CaMnBi<sub>2</sub> [28], Dirac nodal line in HfSiS [29], ZrGeSe [30], ZrGeTe [31], ZrSiTe [32], ZrSiS [33–35], and topological bands in ZrSnTe [36]. In spite of the variety of experimental investigations, however, general descriptions for the topological properties of  $P4/nmm$  materials are still insufficient.

To verify the origin of various topological properties of  $P4/nmm$  materials, we show that the extended TB model with distant-neighbor hoppings is needed to capture the main features of the Fermi surface topology. We also show that the electron-hole ( $e-h$ ) asymmetry and chemical potential play crucial roles in Fermi surface topologies of  $P4/nmm$  materials in the presence of spin-orbit coupling (SOC). Based on the low-energy band structures and TB model, we classify the most reported  $P4/nmm$  materials into the phase diagram of Fermi surface topologies. Lifshitz transition observed in spectroscopy and all the reported SdH oscillation results are consistent with our phase diagram. We also predict the possible modulation of Fermi surface topologies for  $P4/nmm$  materials near the phase boundary.

**II. TIGHT BINDING ANALYSIS**

Based on the DFT calculations on  $P4/nmm$  materials (Fig. 8 in Appendix), we confirmed that the low-energy band structures of those materials are nearly two-dimensional and showing nodal-line feature. Additionally, those low-energy

\*jshim@postech.ac.kr

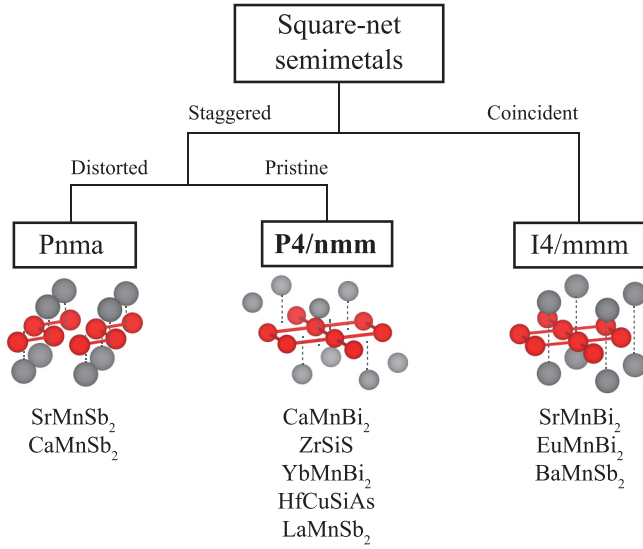


FIG. 1. Families in square-net semimetals according to crystal structures and space group.  $Pnma$  and  $P4/nmm$  materials have staggered stacking of cation atoms (designated as gray spheres) above and below square-net atoms (designated as red spheres), whereas  $I4/mmm$  materials have coincident stacking.  $Pnma$  materials with staggered stacking have CDW distortion of square-net layer.

band structures are dominated by  $p_{x,y}$  orbitals of square-net-layer atoms. Therefore, we investigate the two-dimensional TB model of the single square-net lattice, and the detailed derivation of TB model are shown in the Appendix.

The minimal TB Hamiltonian for square-net pnictogen with a basis set of  $p_{x,y}$  orbitals and the nearest-neighbor (NN)

hoppings is expressed as [15]

$$H^{NN}(k) = t^{10} \cos \frac{k_x}{2} \cos \frac{k_y}{2} \tau_1 \otimes \sigma_0 + t^{11} \sin \frac{k_x}{2} \sin \frac{k_y}{2} \tau_1 \otimes \sigma_1, \quad (1)$$

where  $\tau, \sigma$  are Pauli matrices of site and orbital spaces,  $(k_x, k_y)$  are crystal momentum vectors, and  $\{t^{10}, t^{11}\}$  are model parameters. This minimal TB model produces the band structure containing nodal line touching the BZ boundary as shown in Figs. 2(a) and 2(e).

Based on the orbital character analysis, it is known that the next-nearest-neighbor (NNN) and the third-nearest-neighbor (TNN) hoppings are mediated by the  $s$  orbital of in-plane atoms, and they can be expressed as

$$H^{NNN}(k) = \frac{\Delta}{4} (\cos k_x - \cos k_y) \tau_0 \otimes \sigma_3, \\ H^{TNN}(k) = E_{ch} (\sin k_x - \sin k_y) \tau_0 \otimes \sigma_1, \quad (2)$$

with  $\Delta$  of the energy gap at X point, and  $E_{ch}$  of  $e$ - $h$  asymmetry. The NNN hopping opens the energy gap at X point, so the nodal line does not cross BZ boundary anymore as shown in Figs. 2(b) and 2(f). The nodal line produced by NN- and NNN-hoppings yields trivial Berry phase [15,37]. The TNN hopping breaks the  $e$ - $h$  symmetry because  $\tau_0 \otimes \sigma_1$  is not anticommutative with  $H^{NN}$  and  $H^{NNN}$ . So, it generates electron and hole pockets as shown in Figs. 2(c) and 2(g). The linear band crossing points on  $\Gamma$ -X lines are denoted by  $X'$  as shown in Figs. 2(c) and 2(d).

When the cation atoms stack above and below the square-net layer with staggered stacking, the degeneracy at nodal line is lifted in the existence of the SOC. The  $d$  orbitals of stacking atoms interact with  $p$  orbitals of square-net atoms to produce

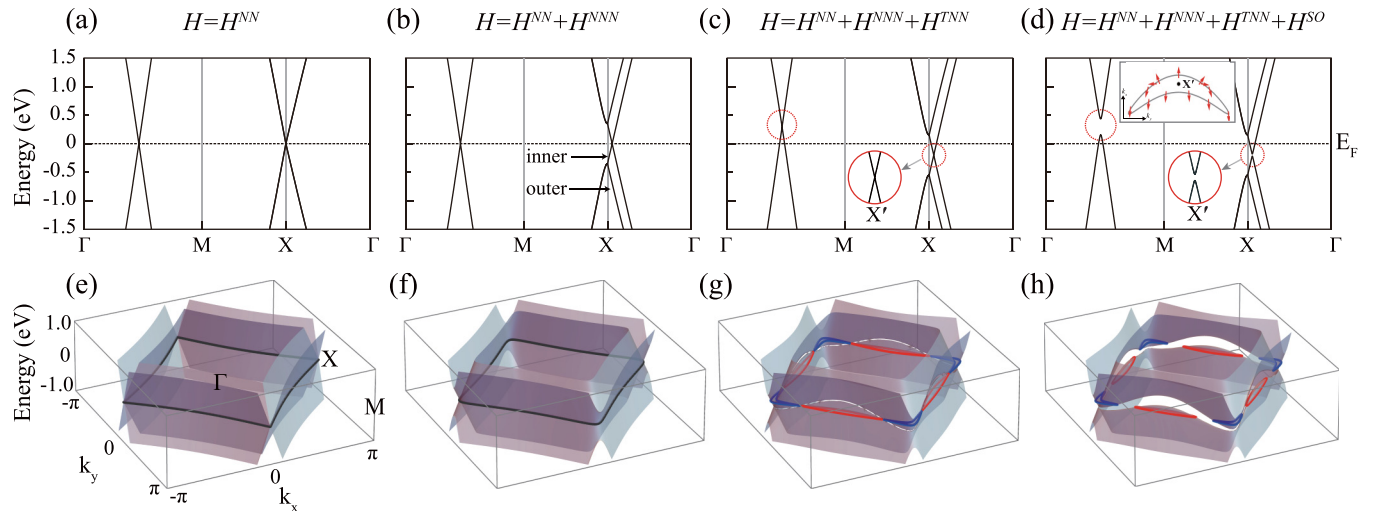


FIG. 2. Band structures of TB models. (a)–(d) Band structures along high symmetry lines. (e)–(h) Two-dimensional band structures over whole BZ. The band structures are reproduced from the TB Hamiltonian with the NN hopping [(a) and (e)], up to the NNN hopping [(b) and (f)], up to the TNN hopping [(c) and (g)], and up to the TNN hopping and Kane-Mele SOC [(d) and (h)]. In (c) and (d), the red circles highlight the SOC band gap. In (e) and (f), black solid lines indicate two-dimensional Fermi surfaces. In (e), the Fermi surface touches BZ boundary, but does not in (f) due to the energy gap opening at X point. In (g), the blue and red lines indicate electron and hole pockets, respectively, and the SOC gap at the nodal line splits the Fermi surface into separated pockets in (h). Inset of (d) shows the pseudospin character of the effective Hamiltonian of low-energy band near  $X'$ .

the Kane-Mele SOC as [37]

$$H^{SO}(k) = \lambda \tau_3 \otimes \sigma_1 \otimes (\sin k_x s_1 - \sin k_y s_2), \quad (3)$$

with the third Pauli matrix  $s_i$  of spin space. As shown in Fig. 2(d), the SOC opens the energy gap at nodal line, forming the separated electron and hole pockets.

The essential features of Fermi surfaces of the square-net materials can be reproduced by the TB Hamiltonian with the distant-neighbor hoppings and Kane-Mele SOC:

$$H = H^{NN} + H^{NNN} + H^{TNN} + H^{SO}. \quad (4)$$

As  $H^{TNN}$  and  $H^{SO}$  are included, the Fermi surface is split into individual pockets [Fig. 2(h)], the cyclotronic orbits on Fermi surfaces are well defined, and Berry phase of each pocket can be identified.

### III. BERRY PHASE OF LOW ENERGY BANDS

As shown in Fig. 2(d), there are the four electron (hole) pockets at  $X'$  and other four hole (electron) pockets on  $\Gamma$ -M lines. As the main source of the Berry phase is shown at  $X'$  pockets [37], the effective Hamiltonian around  $X'$  with Kane-Mele SOC becomes

$$H_{\text{eff}}(q) = \pm v_x q_x (\sigma_3 \otimes \sigma_0) + \lambda q_y (\sigma_1 \otimes \sigma_2) \mp \lambda \sin K (\sigma_1 \otimes \sigma_1), \quad (5)$$

where  $v_x$  is the effective Fermi velocity along  $x$  axis and  $q$  is the momentum vector relative to  $X' = (K, 0)$ . The three terms in the effective Hamiltonian satisfy the anticommutation relations. Therefore, it can be regarded as a two-dimensional massive Dirac Hamiltonian with the first and second terms as the momentum of Dirac fermion, and the third term as a mass. The inset of Fig. 2(d) shows the pseudospin characters ( $\sigma_3 \otimes \sigma_0, \sigma_1 \otimes \sigma_2$ ) of the effective Hamiltonian around  $X'$  point. The pseudospin winding of effective Dirac fermion shows a nontrivial Berry phase of the  $X'$  pocket.

The chemical potential and  $e$ - $h$  asymmetry determine whether the Fermi surface encloses  $X'$  point or not, and whether to give nontrivial or trivial Berry phase assuming SOC gap is very small. As shown in Fig. 3(a) and 3(b), there are two band-crossing points along  $\Gamma$ - $X$  and  $\Gamma$ - $M$  lines. If the Fermi level lies between two energy levels of the crossing points [region (II) or (II')] in Figs. 3(a) and 3(b)], four electron pockets and four hole pockets appear as shown in Fig. 3(d). Then, the pockets are disconnected from each other, hence the pockets around  $X'$  points yield nontrivial Berry phase in SdH oscillations. On the contrary, if Fermi level lies above or below both of two crossing energy levels [region (I) or (III)], all pockets are connected as shown in Figs. 3(c) and 3(e), and yield trivial Berry phase [37]. These results are summarized in the Table I.

### IV. CLASSIFICATION OF FERMION SURFACE

Our investigation can be generalized to three-dimensional Fermi surface with the energy dispersion along the  $k_z$  direction by interlayer interactions. The topologies of Fermi surface cross sections on  $k_x$ - $k_y$  plane can be changed as  $k_z$  value of the plane changes. Due to the symmetry of the crystal structure, Fermi surface of  $P4/nmm$  material has a mirror-symmetric

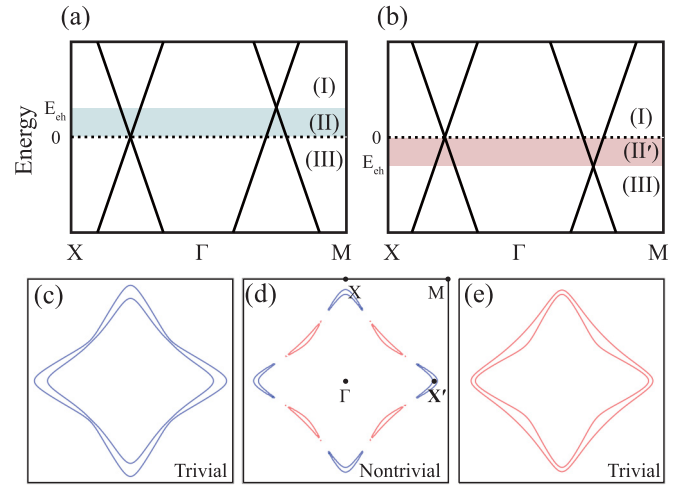


FIG. 3. Schematic band structure of  $P4/nmm$  materials with (a)  $E_{\text{ch}} > 0$  and (b)  $E_{\text{ch}} < 0$ . If the chemical potential lies in region (II) or (II'), it yields nontrivial Berry phase. (c)–(e) Topologically nontrivial and trivial Fermi surfaces of ZrSiSe depending on the chemical potentials, which correspond to (I), (II), and (III) in (a), respectively.

shape with respect to the  $k_z = 0$  and  $k_z = \pm\pi$  planes. Hence, the Fermi surface has extremal cross-sectional area on  $k_z = 0$  and  $k_z = \pm\pi$  planes, where SdH oscillations are observed.

Figure 4 shows the phase diagram of Fermi surface topologies with respect to the  $E_{\text{ch}}$  and  $\mu$  denoted in Fig. 3 and Table I. In the phase diagram, the blue and red regimes indicate nontrivial Berry phase at  $X'$  point, while the white regime indicates trivial Berry phase.

Although there are a total of sixteen types of Fermi surfaces, they can be reduced to six types by switching  $k_z = 0$  and  $k_z = \pi$  planes, or switching electron and hole pockets, which does not change the Fermi surface topology. Figures 4(a)–4(f) show the six possible types by Fermi surface topologies on  $k_z = 0$  and  $k_z = \pm\pi$  planes. The change of Fermi surface topology is represented using gray arcs in the phase diagram with filled and open circles indicating  $k_z = 0$  and  $k_z = \pm\pi$  planes, respectively. If both filled and open circles are located in the same regime in the phase diagram, the Fermi surfaces would be nearly cylindrical [Figs. 4(a) and 4(e)]. If each circle is located in different regimes, the Fermi surfaces show different Berry phases in each  $k_z = 0$  and  $k_z = \pm\pi$  planes. Figures 4(a) and 4(b) show the Fermi surfaces that are trivial

TABLE I. Electronic and topological property of two-dimensional TB Hamiltonian for  $P4/nmm$  materials from  $E_{\text{ch}}$  and  $\mu$ .

$E_{\text{ch}}$	$\mu$	$X'$ pocket	Berry phase
+	$\mu < 0$	hole	Trivial
	$0 < \mu < E_{\text{ch}}$	electron	Nontrivial
	$E_{\text{ch}} < \mu$	electron	Trivial
-	$\mu < E_{\text{ch}}$	hole	Trivial
	$E_{\text{ch}} < \mu < 0$	hole	Nontrivial
	$0 < \mu$	electron	Trivial

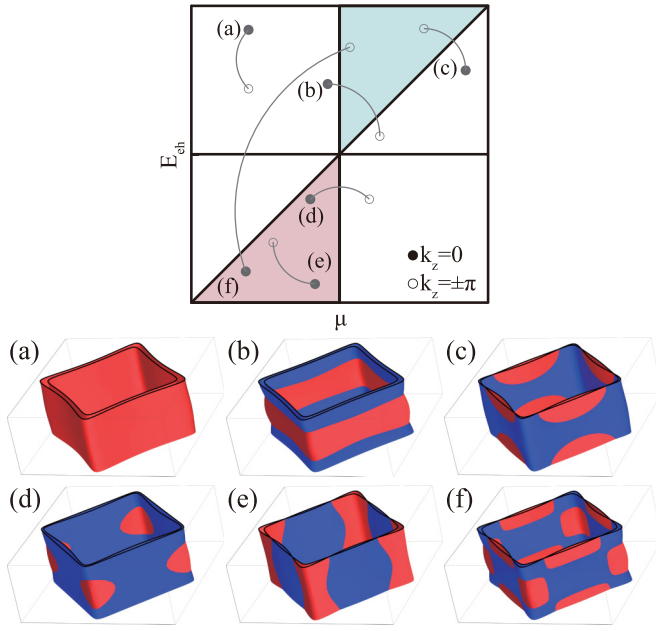


FIG. 4. Schematic phase diagram including  $z$ -axis dispersions. Filled circles and open circles indicate  $k_z = 0$  and  $\pm\pi$  planes, respectively. (a)–(f) Three-dimensional Fermi surface with different topologies on  $k_z = 0$  and  $k_z = \pm\pi$  planes. The Berry phases from SdH experiment are trivial in (a) and (b), and nontrivial in (c) and (f). Note that our classification is up to exchanging two planes or electrons/hole pockets, and SOC gap is not presented.

on both planes; that results in trivial Berry phases in SdH oscillations. Figures 4(c) and 4(d) show the Fermi surfaces

that are trivial on one plane and nontrivial on the other plane. In these cases, both trivial and nontrivial Berry phases of SdH oscillations are observed. In Figs. 4(e) and 4(f), on the other hand, both  $k_z = 0$  and  $k_z = \pm\pi$  planes are nontrivial. Then, at least two distinct nontrivial Berry phases are observed in SdH oscillations, each from  $k_z = 0$  and  $k_z = \pm\pi$  plane.

## V. PHASE DIAGRAM OF $P4/nmm$ MATERIALS

We perform DFT calculation for a total of 31  $P4/nmm$  materials in ZrSiS, HfCuGeAs, and CaMnBi<sub>2</sub>-types (Fig. 8 in Appendix and Table II). We use full-potential linearized augmented plane wave method with WIEN2k package [43], and we use Perdew-Burke-Ernzerhof generalized gradient approximation (PBE-GGA) functional [44]. The number of  $k$  points in the first Brillouin zone (BZ) are 5000 with  $RK^{\max}$  of 7.0. For the materials with magnetic ordering of Mn or rare earth elements, the open-core approximation is adopted by treating the localized  $3d/4f$  orbitals as core states. We then extracted the  $\mu$  and  $E_{ch}$  from the calculated DFT band structures of  $P4/nmm$  materials.

We show the phase diagram of the Fermi surface topology with respect to  $e$ - $h$  asymmetry and the chemical potential in Fig. 5, assuming that the magnetic field is oriented along  $z$  axis. Each numbered point in the phase diagram indicates the Fermi surface topology of  $P4/nmm$  materials. Figures 5(a) and 5(b) represent the Fermi surface topologies on  $k_z = 0$  and  $k_z = \pm\pi$  plane, respectively. The blue and red regimes designate nontrivial Berry phase of the Fermi surface, and the white regimes designate trivial Berry phase. The Fermi surface topologies from DFT band structure and SdH oscillation results are summarized in Table II. HfGeSe and HfSiTe are

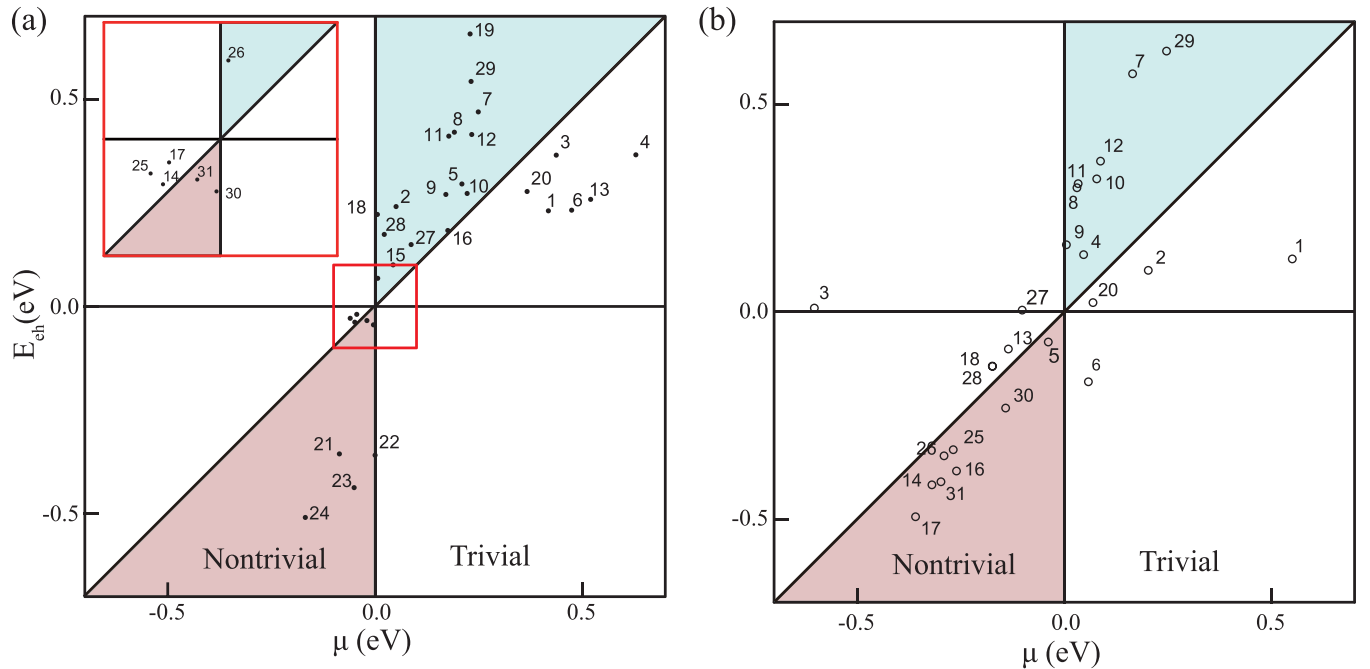


FIG. 5. Phase diagram of the Fermi surface topology on (a)  $k_z = 0$  plane and (b)  $k_z = \pm\pi$  plane, with respect to the chemical potential  $\mu$  and the  $e$ - $h$  asymmetry  $E_{ch}$ . The blue/white regimes indicate nontrivial/trivial Berry phase of the Fermi surface. Each point and number in the phase diagram indicate the square-net materials in Table II, and the points are obtained from the DFT band structure. The SOC is not included in the phase diagram.

TABLE II. Summary of the Fermi surface topologies and SdH experimental results for square-net materials. Type (in fifth column) corresponds to Fig. 3, and T/N denote trivial/nontrivial Berry phase, respectively.

No.	Material	Berry phase at $k_z = 0$	Berry phase at $k_z = \pm\pi$	Type	SdH results
1	CaBe <sub>2</sub> Ge <sub>2</sub>	T	T	a	
2	CaMnBi <sub>2</sub>	N	T	d	N [17]
3	LaMnSb <sub>2</sub>	T	T	a	
4	YbMnSb <sub>2</sub>	N <sup>b</sup>	N <sup>b</sup>	e <sup>b</sup>	N [19]
5	YbMnBi <sub>2</sub>	N	N	f	N [5]
6	LaLiBi <sub>2</sub>	T	T	b	
7	HfCuSiAs	N	N	e	
8	HfCuGeAs	N	N	e	
9	TiCuGeAs	N	N	e	
10	TiCuSiAs	N	N	e	
11	ZrCuGeAs	N	N	e	
12	ZrCuSiAs	N	N	e	
13	CeSbTe	T	T	b	
14	HfGeS	T	N	c	
15	HfGeSe	N	N	f	
16	HfGeTe	N	N	f	
17	HfSiS	T	N	c	N [20]
18	HfSiSe	N	T	d	
19	HfSiTe	N	N	e	
20	LaSbTe	T	T	a	T [16]
21	NbGeAs	N	a	a	
22	NbGeSb	N	a	a	
23	NbSiAs	N	a	a	
24	TaSiAs	N	a	a	
25	ZrGeS	T	N	c	
26	ZrGeSe	N	N	f	N [21]
27	ZrGeTe	N	T	d	N [21]
28	ZrSiSe	N	T	d	N [22]
29	ZrSiTe, (<3 Gpa)	N	N	e	N [22]
	ZrSiTe, (3–8 Gpa)	N	T	d	
	ZrSiTe, (>8 Gpa)	T	T	c	
30	ZrSnTe	N	N	e	N [23]
31	ZrSiS	N	N	e	N [22,24],/T [33]

<sup>a</sup>Omitted due to a lack of two-dimensional features.

<sup>b</sup>Magnetic  $d/f$  orbitals are included.

not shown in Fig. 3(b), because their  $\mu$  and  $E_{\text{ch}}$  are out of the Phase diagram. ( $\mu$ ,  $E_{\text{ch}}$ ) of HfGeSe and HfSiTe are  $(-0.30, -0.84)$ ,  $(0.37, 0.88)$ , respectively. All the reported SdH oscillation results of Berry phases agree well with our prediction: trivial for LaSbTe and nontrivial for most other materials.

Note that if Fermi surface is located close to boundary of regime in the phase diagram, its topologies can be changed by small perturbations. When the chemical potential is changed by chemical doping assuming rigid-band approximation, it is represented as the horizontal movement in the phase diagram. Fermi surface topologies can be sensitively changed by chemical doping. For example, the Fermi surface topologies of ZrSiS can be easily changed by shifting the chemical potential by 20 meV (Fig. 5). This is less than 0.5% of the band width or 0.02 electrons per one formula unit.

## VI. TEMPERATURE- AND PRESSURE-INDUCED LIFSHITZ TRANSITION

The transport anomalies of ZrSiSe were observed by scanning tunneling microscopy measurements, and they are

interpreted by the transition of Fermi surface topology induced by Fermi level shift of  $\sim 0.1$  eV as temperature changes [38]. Our analysis based on the phase diagram shown in Fig. 5 is consistent with the observed transition.

In addition, the pressure-induced transitions of Fermi surface topology of ZrSiTe were observed by infrared and Raman spectroscopy measurements [39,40]. To show the effects of external pressure on Fermi surface topology, we performed DFT calculation of ZrSiTe at hydrostatic pressure of 0 to 10 GPa with intervals of 1 GPa. We used the Vienna *ab initio* simulation package (VASP) in the projector augmented waves (PAW) formalism with PBE functional. The k mesh used in the first BZ is  $20 \times 20 \times 12$ . The atomic positions and lattice are allowed to be fully relaxed.

The band structures of ZrSiTe at various pressures are shown in Fig. 6. The band-crossing points are designated by red and blue circles. When the pressure changes from 0 to 5 GPa, the Z-R pockets changes from electron to hole pockets. In addition,  $\Gamma$ -X electron pocket and A – Z hole pocket at 5 GPa change to hole and electron pockets, respectively, at 10 GPa.

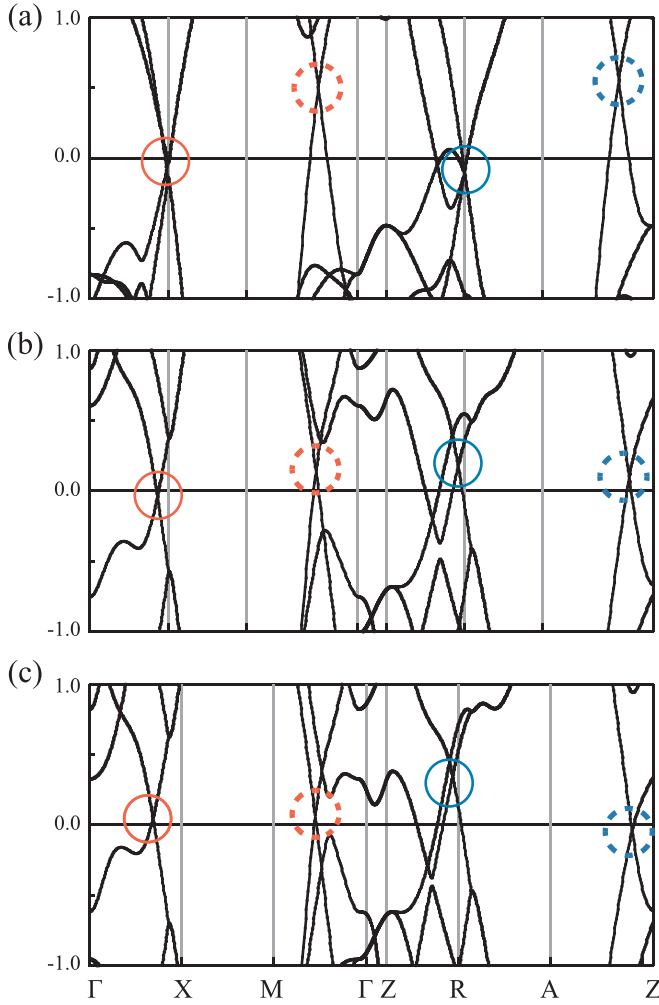


FIG. 6. Band structure of ZrSiTe at pressures of 0, 5, and 10 GPa. Dotted circles indicate  $\Gamma$ -M (Z-A) pockets. Red and blue circles indicate  $k_z = 0$  and  $k_z = \pi$  planes, respectively.

The phase diagrams corresponding to the band structure of ZrSiTe are shown in Fig. 7. Because the  $c$  axis of cell parameter is more sensitive to external pressure than the  $a$  axis, the Fermi surface changes on  $k_z = \pi$  plane rather than  $k_z = 0$  plane. At ambient pressure, both cross sections of

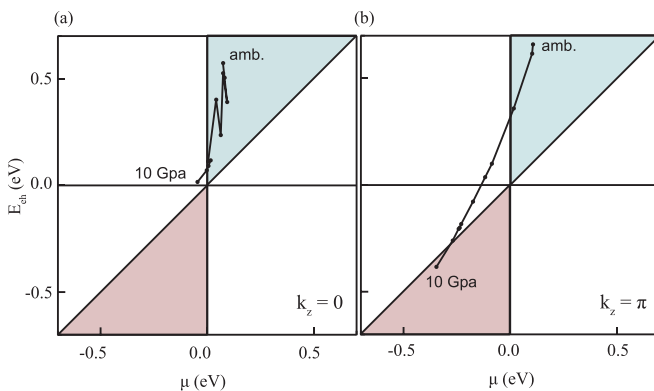


FIG. 7. The phase diagram of ZrSiTe at  $k_z = 0$  (left) and  $k_z = \pi$  (right) at pressure of 0 to 10 GPa. Here, the spin-orbit coupling is ignored.

Fermi surface in blue regime in the phase diagram, hence, the Fermi surface belongs to type  $e$  in Fig. 4. When the pressure exceeds 3–4 GPa, the cross section at  $k_z = \pi$  plane changes the topology, and the Fermi surface belongs to type  $d$ . When the pressure is higher than 8 GPa, the Fermi surface belongs to type  $a$  or type  $c$ . The Lifshitz transitions of ZrSiTe observed by Raman spectroscopy and infrared spectroscopy appear at  $\sim 4.1$  and  $\sim 6.5$  GPa [39,40].

Note that we ignore the SOC of ZrSiTe, and there are quantitative differences of transition pressure between the experimental observations and our investigation. If the SOC is included, the nontrivial regime in the phase diagram shrinks as much as the SOC gap. In the margin of the regimes, the Fermi level lies within the SOC gap and the pockets disappear, hence, Berry phase cannot be nontrivial. This may happen when the cross section is located on the boundary of the phase diagram, such as the 6–9 GPa cases in Fig. 7(a) and 9–10 GPa cases in Fig. 7(b). However, our investigation of ZrSiTe based on the phase diagram reproduces the experimental results qualitatively.

## VII. CONCLUSIONS

In summary, we clarified the origin of nontrivial Berry phase of  $P4/nmm$  materials where the TNN hoppings have important role in the  $e$ - $h$  asymmetry to yield various Fermi surface topologies. We showed that the  $e$ - $h$  asymmetry and chemical potential determines Fermi surface connectivity and Berry phase as SOC is included. Furthermore, phase diagram of the Fermi surface topologies well reproduces the reported SdH experimental results and Lifshitz transition in spectroscopy measurements. Our work provides useful guidelines for interpreting SdH oscillation of  $P4/nmm$  materials.

## ACKNOWLEDGMENT

This work was supported by the Samsung Science and Technology Foundation (Grant No. BA-1501-51).

## APPENDIX

### 1. DFT calculation

We divided the  $P4/nmm$  materials into three types based on structural arrangements: ZrSiS, HfCuGeAs, and CaMnBi<sub>2</sub>-types as shown in Figs. 8(a)–8(c). The three types of the compounds commonly have the square-net atoms (red spheres), and their neighboring atoms (gray spheres) are staggered stacking above and below the square-net layer. The low-energy band structures of the three types are dominated by  $p_{x,y}$  orbitals of square-net layer atoms as shown in Figs. 8(e)–8(g). Their low-energy band structures are highly two-dimensional, and they show nodal-line features.

Note that, there are two main differences in the three band structures shown in Figs. 8(e)–8(g): the energy gap at X point and the difference of two crossing levels on  $\Gamma$ -X and  $\Gamma$ -M lines. The former is explained by next-nearest-neighbor (NNN) hoppings mediated by the stacking metal atoms designated as the gray spheres in Figs. 8(a)–8(c) [37]. The origin of the latter, however, has not been clearly verified.

The single square-net Sb layer and its band structure are shown in Figs. 8(d)–8(h). The electronic structure of the single

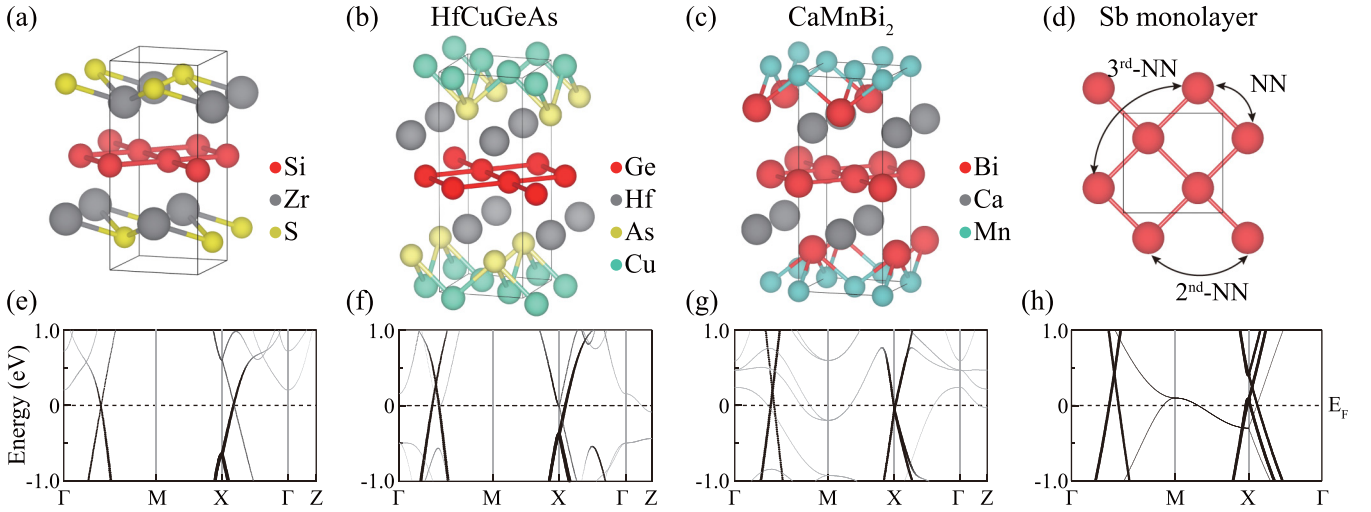


FIG. 8. (a)–(c) Crystal structures of  $P4/nmm$  materials with square-net layers. (a) ZrSiS, (b) HfCuGeAs, and (c) CaMnBi<sub>2</sub>. (e)–(g) Band structures corresponding to each compounds. (d) Crystal structures and (h) band structure of single Sb layer. In (d),  $\sqrt{2} \times \sqrt{2}$  supercell is denoted. In the band structures, the size of the points indicates  $p_{x,y}$  orbital characters of square-net atoms designated as the red spheres in (a)–(d).

layer reproduces the nodal-line and highly two-dimensional features. We obtain maximally localized Wannier functions and their hopping amplitudes using the WANNIER90 code [41,42]. We verify that  $p$  orbital bands are weakly hybridized with  $s$  orbitals of single layer bands, and the distant-neighbor hoppings are mediated by  $s$  orbitals.

## 2. The minimal TB model

Here, we deduce the minimal TB Hamiltonian of square-net pnictogen layer with only NN hoppings. There are two atoms in unit cell at A/B sites and  $p_{x,y}$  orbitals in each atom. The basis set of the TB Hamiltonian is written as

$$\Psi(R) = (p_x^A(R), p_y^A(R), p_x^B(R), p_y^B(R))^T. \quad (\text{A1})$$

Then, the minimal TB Hamiltonian with respect to this basis set is

$$H_0 = \sum_{R,R'} \Psi(R)^\dagger V_0(R, R') \Psi(R'). \quad (\text{A2})$$

Here, for A/B site in unit cell,  $V_0(R, R')$  is determined by Slater-Koster (SK) parameters.

This TB Hamiltonian can be represented in crystal momentum space by Fourier transformation as following:

$$H_0 = \sum_k \Psi(k)^\dagger H^{\text{NN}}(k) \Psi(k), \quad (\text{A3})$$

with the Bloch states  $\Psi(k) = (1/\sqrt{N}) \sum_R e^{-ik \cdot R} \Psi(R)$ . Because this TB Hamiltonian is a  $4 \times 4$  matrix, it can be spanned by  $\tau_i \otimes \sigma_j$ , with  $\tau_i$  and  $\sigma_i$  of Pauli matrices for atomic and orbital basis space, respectively. Therefore, the conventional TB Hamiltonian at each  $k$  can be represented as

$$H^{\text{NN}}(k) = t^{10} \cos \frac{k_x}{2} \cos \frac{k_y}{2} \tau_1 \otimes \sigma_0 + t^{11} \sin \frac{k_x}{2} \sin \frac{k_y}{2} \tau_1 \otimes \sigma_1. \quad (\text{A4})$$

Here,  $\{t_{10}, t_{11}\} = \{2(t_{1\pi} + t_{1\sigma}), 2(t_{1\pi} - t_{1\sigma})\}$  are from SK parameters, and the unit cell length is normalized. Note that  $\tau_0 \otimes \sigma_0$  component is excluded because it only changes the global energy level. Without the SOC,  $p_z$  orbitals cannot hybridize with  $p_{x,y}$  orbitals due to the parity with respect to  $z$  reflection. Therefore, we need to consider only the distant-neighbor hoppings between  $p_{x,y}$  orbitals.

## 3. The distant-neighbor hoppings

In terms of perturbation theory, the distant-neighbor hoppings are the second-order perturbations by filled  $s$  orbitals. Therefore, they can be written as

$$V(k) = \Psi(k)^\dagger \frac{V_{\text{sp}}^\dagger(k) V_{\text{sp}}(k)}{\epsilon_p - \epsilon_s} \Psi(k), \quad (\text{A5})$$

with  $\epsilon$  of the orbital energies and  $V_{\text{sp}}$  of the hopping matrix between  $s$  and  $p$  orbitals.

Excluding  $\tau_0 \otimes \sigma_0$  term,  $V(k)$  can be spanned by Pauli matrices, then the effective NNN and TNN hopping terms can be extracted as following:

$$V(k) := H^{\text{NNN}}(k) + H^{\text{TNN}}(k) = \frac{\Delta}{4} (\cos k_x - \cos k_y) \tau_0 \otimes \sigma_3 + E_{\text{eh}} (\sin k_x - \sin k_y) \tau_0 \otimes \sigma_1. \quad (\text{A6})$$

Here,  $\Delta$  is the energy gap at X point, and  $E_{\text{eh}}$  is  $e$ - $h$  asymmetry energy. We verified that the two terms in  $V(k)$  have same form as direct NNN and TNN hopping terms.

## 4. The SOC effect

When the metal atoms stack above and below the square-net layer, the Kane-Mele SOC can be included. The Kane-Mele SOC with  $d$  orbitals from stacking atoms and  $p$  orbitals

of the square-net atoms is written as [37]

$$H^{\text{SO}}(k) \propto \sum_{AB} \psi^B(k)^\dagger V_{pd} V_{dp} \text{SOC}_p \psi^A(k) + \text{H.c.} \\ = \lambda \tau_3 \otimes \sigma_1 \otimes (\sin k_x s_1 - \sin k_y s_2), \quad (\text{A7})$$

with extension to spin space  $s_i$  of the third Pauli matrices,  $V_{dp}$  of the hopping matrix between  $p$  and  $d$  orbitals,  $A, B$  of two sites in unit cell, and  $\psi^A = (p_{x,\uparrow}^A, p_{x,\downarrow}^A, p_{y,\uparrow}^A, p_{y,\downarrow}^A, p_{z,\uparrow}^A, p_{z,\downarrow}^A)^T$ .

Note that the spinless terms like  $H^{\text{NN}}, H^{\text{NKN}},$  and  $H^{\text{TNN}}$  are embedded as  $s_0$  in spin space. In addition, when the spin space is introduced, each band has two-fold degeneracy due to the time-reversal symmetry. Therefore, there are four pairs of two-fold degenerated bands.

### 5. Dirac fermion around band crossing points

Along the pockets near  $X'$  point, two bands cross the Fermi level. To verify Berry phase of the pocket, we derive the effective Hamiltonian for the inner bands.

When  $k_y = 0$ , the Hamiltonian with the NNN hopping without the SOC effect is

$$H(k) = t^{10} \cos \frac{k_x}{2} \tau_1 \otimes \sigma_0 + \frac{\Delta}{4} (\cos k_x - 1) \tau_0 \otimes \sigma_1, \quad (\text{A8})$$

with the band crossing points at  $X'$ :

$$X' := (K, 0) \\ = \left( \arctan \sqrt{\frac{\sqrt{16(E_{\text{ch}})^2 + (t^{10})^2} - 4E_{\text{ch}}}{t^{10}}}, 0 \right). \quad (\text{A9})$$

Here, note that the spin space  $s_i$  is not introduced yet.

At  $X'$ , the eigenstates of inner bands are  $\sqrt{\frac{1}{2}}(0, -1, 0, 1)^T$  and  $\sqrt{\frac{1}{2}}(1, 0, 1, 0)^T$ . Then we can project the Hamiltonian on the space, which is spanned by the eigenstates of inner bands:

$$H_{\text{in}}(k) = U^\dagger H(k) U \\ = \left[ -\frac{\Delta}{4} (\cos k_x - \cos k_y) - t^{10} \cos \frac{k_x}{2} \cos \frac{k_y}{2} \right] \sigma_3. \quad (\text{A10})$$

Here,  $U$  is the projection matrix onto inner-band-space

$$U = \frac{1}{\sqrt{2}} \begin{pmatrix} 0 & 1 \\ -1 & 0 \\ 0 & 1 \\ 1 & 0 \end{pmatrix}. \quad (\text{A11})$$

Note that the Pauli matrix  $\sigma_i$  does not denote orbital space anymore but inner-band-space, as the basis set is transformed by the projection matrix  $U$ . Because we now only care about the inner bands, it is much convenient to deal with the reduced  $2 \times 2$  matrix  $H_{\text{in}}$  rather than the original  $4 \times 4$  Hamiltonian.

When the spin space  $s_i$  is introduced,  $H_{\text{in}}$  and  $U$  are represented as  $H_{\text{in}} \otimes s_0$  and  $U \otimes s_0$  respectively. Hence, the Kane-Mele SOC can be projected onto inner-band-space as following:

$$H_{\text{in}}^{\text{SO}}(k) = (U^\dagger \otimes \sigma_0) H^{\text{SO}}(k) (U \otimes \sigma_0) \\ = \frac{1}{2} \lambda \sigma_1 \otimes (-\sin k_x \sigma_1 + \sin k_y \sigma_2). \quad (\text{A12})$$

Around  $\pm X'$ , the effective Hamiltonian with the SOC becomes

$$H_{\text{eff}}(q) = \pm v_x q_x (\sigma_3 \otimes \sigma_0) + \lambda q_y (\sigma_1 \otimes \sigma_2) \\ \mp \lambda \sin K (\sigma_1 \otimes \sigma_1), \quad (\text{A13})$$

where  $v_x = \frac{1}{2} t^{10} \sin(\frac{K}{2}) + E_{\text{ch}} \sin K$  and  $\{k_x, k_y\} = \{K + q'_x, q'_y\}$ . The first term is from  $H_{\text{in}}(k)$  and the second and the third are from  $H_{\text{in}}^{\text{SO}}(k)$ .

In the same way, we can also deduce the effective Hamiltonian around  $Y' = (0, K)$  on  $k_y$  axis:

$$H'_{\text{eff}}(q') = \pm v_x q'_y (\sigma_3 \otimes \sigma_0) - \lambda q'_x (\sigma_1 \otimes \sigma_2) \\ \pm \lambda (\sin K \otimes \sigma_1), \quad (\text{A14})$$

with  $\{k_x, k_y\} = \{q'_x, K + q'_y\}$ .

The pockets around  $X'$  have nontrivial Berry phase. The Berry phases for  $X'$  and  $Y'$  have same absolute values.

### 6. 3D dispersion effect

DFT calculations show that the low-energy band structures of  $P4/nmm$  materials on  $k_z = \pi$  planes keep nodal-line features. However,  $E_{\text{ch}}$  and  $\mu$  on  $k_z = 0$  and  $k_z = \pi$  are different due to interlayer interactions. We introduced the simplest  $k_z$ -dependent terms of chemical potential and  $e$ - $h$  asymmetry to take into account the interlayer interaction:

$$H_{3\text{D}}(q') = -\mu_z \cos k_z \tau_0 \otimes \sigma_1 \\ + E'_{\text{ch}} \cos k_z (\sin k_x - \sin k_y) \tau_0 \otimes \sigma_1. \quad (\text{A15})$$

The second term of  $H_{3\text{D}}$  can be represented by modifying  $E_{\text{ch}}$  to  $E_{\text{ch}}^{3\text{D}}$  in (A6):

$$E_{\text{ch}}^{3\text{D}}(k_z) = E_{\text{ch}} + E'_{\text{ch}} \cos k_z. \quad (\text{A16})$$

Here, we assumed monotonic variation of  $\mu$  and  $E_{\text{ch}}$ , and used cosine function for  $k_z$  dependence.

- [1] M. Z. Hasan and C. L. Kane, *Rev. Mod. Phys.* **82**, 3045 (2010).  
 [2] T. Liang, Q. Gibson, M. N. Ali, M. Liu, R. J. Cava, and N. P. Ong, *Nat. Mater.* **14**, 280 (2015).  
 [3] Y. N. Huang, X. L. Yu, D. Y. Liu, and L. J. Zou, *J. Appl. Phys.* **117**, 17E113 (2015).  
 [4] F. Arnold *et al.*, *Nat. Commun.* **7**, 11615 (2016).

- [5] A. Wang, I. Zaliznyak, W. Ren, L. Wu, D. Graf, V. O. Garlea, J. B. Warren, E. Bozin, Y. Zhu, and C. Petrovic, *Phys. Rev. B* **94**, 165161 (2016).  
 [6] N. J. Ghimire, A. S. Botana, D. Phelan, H. Zheng, and J. F. Mitchell, *J. Phys.: Condens. Matter* **28**, 235601 (2016).



- [7] J. Xiong, S. Kushwaha, J. Krizan, T. Liang, R. J. Cava, and N. P. Ong, *Europhys. Lett.* **114**, 27002 (2016).
- [8] S. Cahangirov, M. Topsakal, E. Aktürk, H. Şahin, and S. Ciraci, *Phys. Rev. Lett.* **102**, 236804 (2009).
- [9] W. Li, M. Guo, G. Zhang, and Y. W. Zhang, *Phys. Rev. B* **89**, 205402 (2014).
- [10] M. Kang *et al.*, *Nat. Mater.* **19**, 163 (2020).
- [11] Y. J. Jo, J. Park, G. Lee, M. J. Eom, E. S. Choi, J. H. Shim, W. Kang, and J. S. Kim, *Phys. Rev. Lett.* **113**, 156602 (2014).
- [12] S. M. Young and C. L. Kane, *Phys. Rev. Lett.* **115**, 126803 (2015).
- [13] J. Park *et al.*, *Phys. Rev. Lett.* **107**, 126402 (2011).
- [14] L. Li, K. Wang, D. Graf, L. Wang, A. Wang, and C. Petrovic, *Phys. Rev. B* **93**, 115141 (2016).
- [15] G. Lee, M. A. Farhan, J. S. Kim, and J. H. Shim, *Phys. Rev. B* **87**, 245104 (2013).
- [16] R. Singha, A. Pariari, B. Satpati, and P. Mandal, *Phys. Rev. B* **96**, 245138 (2017).
- [17] K. Wang, D. Graf, L. Wang, H. Lei, S. W. Tozer, and C. Petrovic, *Phys. Rev. B* **85**, 041101(R) (2012).
- [18] S. Borisenko *et al.*, *Nat. Commun.* **10**, 3424 (2019).
- [19] Y.-Y. Wang, S. Xu, L.-L. Sun, and T.-L. Xia, *Phys. Rev. Mater.* **2**, 021201(R) (2018).
- [20] N. Kumar, K. Manna, Y. Qi, S.-C. Wu, L. Wang, B. Yan, C. Felser, and C. Shekhar, *Phys. Rev. B* **95**, 121109(R) (2017).
- [21] J. Hu, Y. L. Zhu, D. Graf, Z. J. Tang, J. Y. Liu, and Z. Q. Mao, *Phys. Rev. B* **95**, 205134 (2017).
- [22] J. Hu *et al.*, *Phys. Rev. Lett.* **117**, 016602 (2016).
- [23] J. Hu, Y. Zhu, X. Gui, D. Graf, Z. Tang, W. Xie, and Z. Mao, *Phys. Rev. B* **97**, 155101 (2018).
- [24] C. Li, C. M. Wang, B. Wan, X. Wan, H.-Z. Lu, and X. C. Xie, *Phys. Rev. Lett.* **120**, 146602 (2018).
- [25] M. N. Ali, L. M. Schoop, C. Garg, J. M. Lippmann, E. Lara, B. Lotsch, and S. S. P. Parkin, *Sci. Adv.* **2**, e1601742 (2016).
- [26] L. M. Schoop *et al.*, *Sci. Adv.* **4**, eaar2317 (2018).
- [27] A. Topp, M. G. Vergniory, M. Krivenkov, A. Varykhalov, F. Rodolakis, J. L. McChesney, B. V. Lotsch, C. R. Ast, and L. M. Schoop, *J. Phys. Chem. Solids* **128**, 296 (2014).
- [28] Y. Feng *et al.*, *Sci. Rep.* **4**, 5385 (2014).
- [29] C. Chen *et al.*, *Phys. Rev. B* **95**, 125126 (2017).
- [30] Z. Cheng *et al.*, *APL Mater.* **7**, 051105 (2019).
- [31] M. M. Hosen *et al.*, *Phys. Rev. B* **97**, 121103(R) (2018).
- [32] A. Topp, J. M. Lippmann, A. Varykhalov, V. Duppel, B. V. Lotsch, C. R. Ast, and L. M. Schoop, *New J. Phys.* **18**, 125014 (2016).
- [33] X. Wang *et al.*, *Adv. Electron. Mater.* **2**, 1600228 (2016).
- [34] L. M. Schoop, M. N. Ali, C. Straßer, A. Topp, A. Varykhalov, D. Marchenko, V. Duppel, S. S. P. Parkin, B. V. Lotsch, and C. R. Ast, *Nat. Commun.* **7**, 11696 (2016).
- [35] M. Neupane *et al.*, *Phys. Rev. B* **93**, 201104(R) (2016).
- [36] R. Lou *et al.*, *Phys. Rev. B* **93**, 241104(R) (2016).
- [37] S. I. Hyun, I. Lee, G. Lee, and J. H. Shim, *Phys. Rev. B* **98**, 165108 (2018).
- [38] F. C. Chen *et al.*, *Phys. Rev. Lett.* **124**, 236601 (2020).
- [39] J. Ebad-Allah, M. Krottenmüller, J. Hu, Y. L. Zhu, Z. Q. Mao, and C. A. Kuntscher, *Phys. Rev. B* **99**, 245133 (2019).
- [40] M. Krottenmüller *et al.*, *Phys. Rev. B* **101**, 081108 (2020).
- [41] A. A. Mostofi, J. R. Yates, Y.-S. Lee, I. Souza, D. Vanderbilt, and N. Marzari, *Comput. Phys. Commun.* **178**, 685 (2008).
- [42] F. Freimuth, Y. Mokrousov, D. Wortmann, S. Heinze, and S. Blügel, *Phys. Rev. B* **78**, 089902(E) (2008).
- [43] P. Blaha, K. Schwarz, G. K. H. Madsen, D. Kvasnicka, and J. Luitz, *WIEN2K, An Augmented Plane Wave + Local Orbitals Program for Calculating Crystal Properties* (Karlheinz Schwarz, Techn. Universität Wien, Austria, 2001).
- [44] J. Sun, A. Ruzsinszky, and J. P. Perdew, *Phys. Rev. Lett.* **115**, 036402 (2015).